UNIVERSITY of York

This is a repository copy of *Contrast-tuneable microscopy for single-shot real-time imaging*.

White Rose Research Online URL for this paper:
https://eprints.whiterose.ac.uk/164296/

Version: Accepted Version

Article:
Shimizu, Isao, Saikawa, Yoshinori, Uno, Katsunori et al. (2 more authors) (2020) Contrast-tuneable microscopy for single-shot real-time imaging. The European Physical Journal Applied Physics. 30701. ISSN 1286-0050

https://doi.org/10.1051/epjap/2020200101

Reuse
Items deposited in White Rose Research Online are protected by copyright, with all rights reserved unless indicated otherwise. They may be downloaded and/or printed for private study, or other acts as permitted by national copyright laws. The publisher or other rights holders may allow further reproduction and re-use of the full text version. This is indicated by the licence information on the White Rose Research Online record for the item.

Takedown
If you consider content in White Rose Research Online to be in breach of UK law, please notify us by emailing eprints@whiterose.ac.uk including the URL of the record and the reason for the withdrawal request.

White Rose university consortium
Universities of Leeds, Sheffield & York

eprints@whiterose.ac.uk
https://eprints.whiterose.ac.uk/

Contrast-tuneable microscopy for single-shot real-time imaging

Isao Shimizu,[1,*] Yoshinori Saikawa,[1] Katsuhiro Uno,[2] Hideaki Kano,[3] and Seishi Shimizu[4,*]

[1]*Research Institute of Advanced Technology, Inc. 3543-2 Higashi-ishikawa, Hitachinaka-Shi, Ibaraki 312-0052, Japan*

[2]*Department of Media and Telecommunications Engineering, College of Engineering, Ibaraki University, 4-12-1 Naka-Narusawa, Hitachi, Ibaraki 316-8511, Japan*

[3]*Department of Applied Physics, Graduate School of Pure and Applied Sciences, University of Tsukuba, 1-1-1 Tennodai, Tsukuba, Ibaraki 305-8573 Japan*

[4]*York Structural Biology Laboratory, Department of Chemistry, University of York, Heslington, York YO10 5DD, United Kingdom*

*riat-smz@riat.co.jp (IS), seishi.shimizu@york.ac.uk (SS)

Abstract: A novel real image in-line laser holography enables a tuneable image contrast, edge sharpness, and visualization of sub-wavelength structures, using a simple pair of filters and large-diameter lenses that can incorporate higher-order scattered light. Demonstrated also are the accuracy in object sizing and the ease of imaging along the focal depth, based on a single-shot imaging via holographic principle. In addition, the use of broad, collimated laser beam for irradiation has led to a wider field of view, making it particularly useful for an extensive monitoring of, and sweeping search for, cells and microbial colonies and for the real-time imaging of cancer-cell dynamics.

1. Introduction

Despite significant recent progress in biomedical imaging, a direct, real-time and staining-free observation of transparent biological objects that are floating and clumping in solution is still an active area of investigation [1–5]. In addition, imaging capability for of intracellular components and exosomes (which can be as small as 50 – 150 nm) would be beneficial in elucidating their biological roles, functions, and interactions [6–11]. However, well-established methods, such as the confocal laser microscopy and super-resolution fluorescence microscopy [6–11], despite their high resolution, inevitably require staining and/or slicing. On the contrary, the Zernike phase contrast microscopy (ZPCM) [12] does not require staining, yet suffers from the halo effect [13], object size inaccuracy, and a narrow

field of view. Recently, dramatic progress has taken place in staining-free imaging in the burgeoning field of quantitative phase-contrast microscopy [3,4,14–17], such as by differential interference microscopy [18–20], digital holographic microscopy [5,21–24], and holographic interference microscopy [25,26]. However, some crucial challenges remain unresolved, as will be reviewed in the following.

The first challenge is image contrast optimization. The variable phase contrast approach was invented to overcome the cumbersome phase-plate refitting procedure of ZPCM [12], such as Polanret microscopy pioneered by Osterberg [27–30]. The key idea is the selective attenuation of the transmitted beam using a polarizer, to which end the transmitted and scattered beam polarizations had to be made perpendicular to one another [27–30]. This requires four phase filters in total [27–30], all of which had to be zonal in shape, in order to match the annular ring of ZPCM [18]. This made the optical design complex, yet the problem inherent in ZPCM persisted; the phase plates had to be wider than the transmitted beam so as to facilitate the optical alignment [4,18,31]. This has caused some of the scattered beam to "leak" into the transmitted beam [4,18,31] and to interfere with the remainder of the scattered beam, thereby giving rise to the halo artifact, leading to the ambiguity regarding size information [4,18,31].

It is coherent irradiation by laser beam that can simplify the optical setup and phase plate design (a pinhole instead of zonal-shaped) while achieving image clarity and high resolution [15,16]. In contrast to single-shot imaging performed in an 'analogue' manner, quantitative phase imaging, implemented through a wide variety of techniques [5,14,15,20–26], constructs an image from multiple shots recorded digitally at multiple phase differences. Note that these techniques focus on thin phase objects with an emphasis on computational image reconstruction to achieve image clarity [5,14,32,15,20–26]. In contrast, however, our approach, in order to achieve a facile real-time imaging of objects often thicker than the wavelength, is based on a direct image generation without computational reconstruction.

Furthermore, many of the quantitative phase imaging approaches proposed so far focus on lower-order scattered beams [5,14,15,20–26]. However, incorporating higher-order scattered beams is beneficial for image edge clarity and for observing microstructures smaller in scale than wavelength. This is underscored by the success of dark field microscopy, which, through the incorporation of higher-order scattered beams, made it possible to visualize microstructure as small as 90 nm [33]. However, the dark field microscopy not only contains a cumbersome optical construction using cardioid annular condenser but also discards the transmitted beam altogether, leading to limitations in contrast clarity.

Thus, incorporating higher-order scattered beams combined with the facility of analogue contrast optimization via laser irradiation are the key to achieve single-shot, stain-free, imaging of thick, transparent samples, which offers the capacity of observing sub-wavelength microstructures with high contrast and clarity. We report here the design principles, implementation, and performance of such a novel real image in-line holographic microscopy to achieve these aims.

2. Design and setup

Our setup is essentially an in-line holographic microscopy, in which a broad, collimated laser beam is irradiated onto the object (Figure 1(a)(b)). The object beam is the real image, whereas the reference beam is the transmitted light (0^{th} order beam). Coherent laser irradiation is advantageous in attaining (i) a wider field of view by eliminating the annular ring of ZPCM [12,31], (ii) an improved detection of microstructure by incorporating higher-order scattered beam, facilitated by (i), as well as laser's polarization, coherence, and focusability [34], and (iii) a reasonably compact image size, thanks to the lack of need for simultaneous irradiation from multiple directions (and hence scattering into even more diverse directions) caused by the annular ring.

Hence, the main design features are: (1) a wide, collimated and coherent laser irradiation beam (diameter: 20 mm); (2) a large Fourier-transform (FT) and inverse Fourier transform (iFT) lenses (L_1, NA: 0.8, L_2, diameter: 60 mm) for incorporating higher-order scattered beams; (3) a $\lambda/4$ plate (P_3) with a small

pinhole in the middle, allowing the passage of the transmitted (0th order) beam while introducing circular polarization for the scattered beam (Figure 1(c)); a tuneable polarizer (P_4) for image contrast optimization, selectively attenuating the linearly-polarized transmitted beam while passing through the scattered beam (Figure 1(c)). See Appendix for the theoretical basis for contrast optimization.

The laser used for irradiation was purchased from Changchun New Industries Optoelectronics Technology (MLL-III-532-50mW, λ=532 nm, 50 mW). The lenses used for our microscope, whose specifications are listed below, were purchased from the following manufacturers: L_1: Olympus Co. (MPLFLN50X, semi-apochromat, 50×, NA 0.8, W.D. 1 mm, f'_1=45 mm, f_1= 3.6 mm); L_2: Edmund Optics (achromatic lens, D_2=75 mm, f'_2= 200 mm, f_2=187.7 mm); L_3: Tochigi Nikon (D_3=43 mm, f'_3=46 mm, f_3=35 mm); L_4: Tochigi Nikon (D_4=50mm, f'_4=85 mm, f_4=44 mm). The quartz λ/4 filter was purchased from Shibuya Kougaku, (λ=532 nm, Φ50.8). A hole with 0.3 mm in diameter was bored at the centre. Two cameras were used for imaging, indicated in each of our figures via the μm/pixel specification. (i) CCD camera: IPX-11M5-L from Imperx, Inc. (4000×2672 pixels, 9 μm/pixel); (ii) CMOS camera: Genie Nano M2420 Mono from Teledyne DALSA, Inc. (2464×2056 pixels, 3.45 μm/pixel).

Thus, the above setup aims at a real-time recording of holographic information with a wider field of view, incorporating higher-order scattered beams for clearer microstructure imaging, with continuous contrast optimization. In addition to the novel design as summarized above, a secondary optical system consisting of L_3 and L_4 has been added to improve the magnification ratio.

3. Performance

3.1 Sizing objects

Sizing objects accurately, despite its key importance, posed serious challenges to ZPCM due to the halo artifact [31]. To examine the capacity of our microscope, we carried out an imaging of a mixture of mono-disperse polystyrene latex

spheres of three different diameters (5.0, 10.3, and 20.3 μm) as an example (Figure 2(a)). For these spheres, we have obtained 5, 10, and 20 μm, respectively, from the intensity profile across their diameters, calculated from the camera specification of 9 μm/pixel (Figure 2(b)). These evaluations are in close agreement with the diameters quoted by the manufacturer. Here, the optical thickness difference between the center and the edge leads to the appearance of bright and dark rings due to constructive and destructive interferences [34]. Note that the following polystyrene latex spheres were used in the imaging: 20.3 μm: catalogue no. SS-203-P from JSR Life Sciences, Co.; 10.3 μm: catalog no. PS010UM from Magsphere, Inc; 5.0 μm: catalogue no. PS005UM from Magsphere; 0.5 μm: catalogue no. 07307 from Polysciences, Inc. ; 80 nm gold nanoparticle:catalogue no. G-80-20 from Cytodiagnostics, Inc.

Let us examine whether the accurate sizing capability of our microscope remains valid even for smaller objects comparable to the irradiation wavelength (532 nm). To this end, the sample chosen for imaging is a mixture of polystyrene latex spheres (diameter 500 nm) and gold nanoparticles (diameter: 80 nm), as shown in Figure 3(a) (the whole view) and Figure 3(b)(c) (expanded image for a closer examination). Considering that 500 nm and 80 nm correspond to 20 and 3 pixels, respectively, the objects in the image (Figure 3(c)) and the corresponding line profiles (Figure 3(d)) roughly match the calculated pixel sizes.

3.2 Contrast optimization and Image clarify from higher-order scattered light

Our laser microscopy has been designed specially (i) to incorporate higher-order scattered beams by adopting the large-diameter lenses and filters and (ii) to optimize image contrast by the filter pair. These two features do indeed lead to a clearer imaging, as will be shown below.

Firstly, the large size of the lenses and the filter pair can improve the contrast significantly, as has been demonstrated by Figure 4, using the same mixtures of polystyrene and gold particles as before. Indeed, reducing the diameter of iFT lens (L_2 in Figure 1(b), 60mm in diameter) using apertures (45mm, 30mm, and

15mm) leads to the reduction of contrast (Figure 4(a)), which can be appreciated from the resultant images themselves as well as from the intensity profile (Figure 4(c)). Indeed, the lens diameter restriction makes the intensity peak fall below the average intensity, making it harder to detect nanoparticles.

Secondly, image contrast is tuneable in our microscope, by virtue of the polarizer pair. Unlike the conventional ZPCM, it is the transmitted beam that is linearly polarized, while the scattered beam is circularly polarized (Figure 1(c)). Hence the polarizer can attenuate the transmitted beam selectively, while passing through the scattered beam with an additional phase shift. The attenuation factor of the transmitted beam is tuneable by simply rotating the polarizer. This alternative setup (i.e., linear polarization for the transmitted beam) is advantageous both for phase objects and thick objects, enabling our microscope to operate as phase contrast and bright field microscopy. See Appendix for a detailed theoretical exposition on the principle of variable contrast optimization.

Imaging objects smaller in size than irradiation wavelength posed difficulties [33]. However, Figures 3 and 4 demonstrate that such objects can at least be detected, even with some size information. Even though the gold nanoparticles are not transparent and is therefore not a typical object for imaging by phase contrast microscopy, our filter significantly improves the contrast.

We have thus shown that contrast optimization, while incorporating higher-order scattered beams, is beneficial for clear imaging. This is in contrast with the approaches taken by the modern quantitative phase imaging that use lowest-order scattered light exclusively for imaging.

4. Towards biomedical applications

Here we demonstrate the potential of our microscope for biomedical applications, both in terms of the sweeping search and detection, as well as imaging, of individual cells and cellular colonies.

Firstly, searching and detecting objects of interest (such as counting blood cells or stem cell colonies) through a sweeping search would significantly be made efficient by the wide field of view of our microscope as demonstrated in Figure 5(a).

Secondly, the expanded image shown in Figure 5(b) demonstrates that our microscope is capable of single-shot imaging intracellular structure, distinguishing clearly between different types of human blood cells.

Thirdly, our microscope is equipped with a capacity of detecting objects that are off the focal depth. This can be seen clearly by the human oral epithelial cells that were imaged along varying focal depths (by an interval of 0.5 μm) as shown in Figure 6. The persistent visibility of the cell off the focal depth evidences the capacity to carry out facile detection of the cellular objects not only by the wide field of view but also by the object visibility far off the focal depth.

The lack of need for computational image reconstruction is advantageous when imaging objects along time. We shall present here two potential applications that may be promising for biomedical imaging.

The first application is flow cytometry (Figure 5(c)). Conventional flow cytometry employs a narrow tube, through which the trajectory of a single particle can be followed individually one at a time. Such a limitation was necessitated by the use of light scattering for the determination of cellular size and shape where staining plays a crucial role. In stark contrast, the flow cytometry using based on our microscope can be made much more efficient, because it is possible to follow the trajectory of every single cell within the wide field of view at the same time. In addition, staining is no longer necessary, hence our approach enables the non-destructive cytometry of live, flowing cells. The wide field of view facilitates the visualization of human blood cell trajectory while maintaining the ability of visualizing intracellular structures (as demonstrated above).

The second is a stain-free, real-time imaging of live cancer cells. Imaging the time evolution of human lung cancer cell motion (of the A549 cell line, provided by

Professor Masayuki Noguchi of the University of Tsukuba) [35,36], as shown in Figure 7, as a series of snapshots that visualise the signature morphological dynamics of the cancer cell without the need for staining, which may play a crucial role for diagnosis.

Thus, we expect our novel microscope would be a powerful and effective tool for biomedical imaging on a cellular and sub-cellular scale.

5. Conclusion

Biomedical imaging of cellular and intracellular structures [1], as well as a sweeping search of objects in cultures, tissues, and specimens, requires the stain-free, real-time imaging with a wide field of view. To this end, we have developed a novel in-line laser holographic microscope with tuneable contrast, using a simple filter pair, and with the large FT and iFT lenses to incorporate higher-order scattered beams. This has led to real-time imaging with the ability to detect small objects and to evaluate object sizes larger than the wavelength, overcoming the difficulties faced by ZPCM. Moreover, the recovery of images away from the focal plane, as well as the detection of microstructures well-below irradiation wavelength, has been demonstrated, making it an attractive approach for imaging cellular dynamics and conducting a sweeping search for the target cells.

Appendix

Here we illustrate the operational principles of tuneable phase contrast theoretically, taking a transparent phase object an example, based upon Fourier optics and the Jones matrices [8,9]. Here we deal with the simplified optical system in Figure 8(a) which captures the basic principles of contrast optimization. The coordinate systems used in the discussion below are defined in Figure 8(b). Let $F(x,y)$ be the transmission function of a transparent phase object at the position (x,y), expressed as

$$F(x,y) = e^{i\phi(x,y)} \quad (1)$$

where ϕ is the phase of the object. In Figure 8(a), the object plane coincides the front focal plane of the lens L_1. Under this condition, the complex disturbances of the direct and the scattered lights, denoted respectively by $U_0(\xi,\eta)$ and $U_1(\xi,\eta)$

at the position (ξ, η) on the back focal plane of the lens L_1 (Figure 8), can be expressed in terms of the exact Fourier transform relationships under the paraxial approximation, as [8,9]

$$U_0(\xi,\eta) = C_1 \iint dxdy\, P_R(x,y) e^{-\frac{ik(\xi x+\eta y)}{f_1}} \quad (2)$$

$$U_1(\xi,\eta) = C_1 \iint dxdy P_R(x,y)\left[e^{i\phi} - 1\right] e^{-\frac{ik(\xi x+\eta y)}{f_1}} \quad (3)$$

where k is the wavenumber and C_1 is a constant [7]. Here, $P_R(x,y)$ represents the pupil function of an aperture of radius R, namely $P_R(x,y) = 1$ for $x^2 + y^2 \leq R$ and = 0 otherwise. When R is sufficiently large, we can set $P_R(x,y) = 1$ over the entire range of integration in Eqs. (2) and (3) [8,9].

Subsequently, the scattered beam travels through both the $\lambda/4$ phase plate (P_1) and the polarizer, whereas the transmitted beam passes through the aperture in the middle of the $\lambda/4$ phase plate (P_1) before travelling through the polarizer. Hence a careful consideration of the polarization vectors of both the scattered and the transmitted beams is indispensable to calculate the image intensity on the image plane. For simplicity, let the irradiation beam be linearly polarized at an angle $\pi/4$ to the axis of the $\lambda/4$ phase plate (x-axis), and the polarizer passes the wave component polarized at an angle α from the same axis. Using the Jones matrix for the polarizer, transmitted beam after the polarizer can be expressed as [9]

$$\begin{pmatrix} \cos^2\alpha & \sin\alpha\cos\alpha \\ \sin\alpha\cos\alpha & \sin^2\alpha \end{pmatrix} \frac{1}{\sqrt{2}} \begin{pmatrix} 1 \\ 1 \end{pmatrix} = \sin\left(\alpha + \frac{\pi}{4}\right) \begin{pmatrix} \cos\alpha \\ \sin\alpha \end{pmatrix} \quad (4)$$

The scattered beam after the $\lambda/4$ phase plate (with transmission coefficient b) and the polarizer can be expressed as

$$\begin{pmatrix} \cos^2\alpha & \sin\alpha\cos\alpha \\ \sin\alpha\cos\alpha & \sin^2\alpha \end{pmatrix} b \begin{pmatrix} 1 & 0 \\ 0 & -i \end{pmatrix} \frac{1}{\sqrt{2}} \begin{pmatrix} 1 \\ 1 \end{pmatrix} = \frac{b}{\sqrt{2}} e^{-i\alpha} \begin{pmatrix} \cos\alpha \\ \sin\alpha \end{pmatrix} \quad (5)$$

Because the two beams after the polarizer has the same polarization, from now onwards we consider only the $\begin{pmatrix} \cos\alpha \\ \sin\alpha \end{pmatrix}$ component of the transmitted and scattered beams, by multiplying the factors $\sin\left(\alpha + \frac{\pi}{4}\right)$ and $\frac{b}{\sqrt{2}} e^{-i\alpha}$ to their respective disturbances.

Now the image plane (in Figure 8(a)) is adjusted to coincide with the back focal plane of the lens L_2, while P_1 is the front focal plane of the same lens. At the

position (x', y') on the image plane, the disturbances of the transmitted and the scattered beams, denoted respectively as $V_0(x', y')$ and $V_1(x', y')$, can be expressed using Fourier transforms [8,9], together with the effect of polarizer described by Eqs. (4) and (5), as

$$V_0(x', y') = C_2 \sin\left(\alpha + \frac{\pi}{4}\right) \iint d\xi d\eta U_0(\xi, \eta) e^{-\frac{ik(\xi x' + \eta y')}{f_2}} = C \sin\left(\alpha + \frac{\pi}{4}\right) \quad (6)$$

$$V_1(x', y') = C_2 \frac{b}{\sqrt{2}} e^{-i\alpha} \iint d\xi d\eta U_1(\xi, \eta) e^{-\frac{ik(\xi x' + \eta y')}{f_2}}$$

$$= C \frac{b}{\sqrt{2}} e^{-i\alpha} \left[F\left(-\frac{x'}{M}, -\frac{y'}{M}\right) - 1\right] \quad (7)$$

where C_2 and C are constants common to Eqs. (6) and (7), and $M = f_2/f_1$ [8]. Using Eqs. (1), (6) and (7), the intensity on the image plane can be expressed as

$$|V(x', y')|^2$$

$$= |C|^2 \left[\sin^2(\alpha + \tfrac{\pi}{4}) + 2\sqrt{2}b \sin(\alpha + \tfrac{\pi}{4}) \sin\tfrac{2\alpha - \phi}{2} \sin\tfrac{\phi}{2} + 2b^2 \sin^2\tfrac{\phi}{2}\right] \quad (8)$$

Since $\phi \ll 1$, taking up to the first order of ϕ, Eq. (8) can be simplified as

$$|V(x', y')|^2$$

$$\simeq |C|^2 \left[\sin^2\left(\alpha + \frac{\pi}{4}\right) + \sqrt{2}b\phi \sin\left(\alpha + \frac{\pi}{4}\right) \sin\alpha\right] \quad (9)$$

Contrast optimization in our microscope thus involves the rotation of the polarizer (i.e., changing the angle α), as has been shown by Eq. (9). When α is close to $-\pi/4$, the first term can be made one order of magnitude smaller than the second term which contains the phase information, enhancing the contrast in principle. However, it is important to note, in practice, that $\alpha \simeq -\pi/4$ also makes the phase image (i.e., the second term of Eq. (9)) weak, which leads to a dark image. Taken all together, the optimum contrast can be found by varying the angle α, to seek a balance: attenuating the transmitted beam while keeping the phase image sufficiently bright. This is demonstrated using polystyrene spheres in Figure 8(c), showing that rotating the polarizer indeed lead to contrast variation.

In contrast to our approach, tuneable contrast optimization was not possible in ZPCM. According a well-known formula [8], the image intensity of ZPCM can be expressed as $|C|^2 a^2 \left(1 \pm \frac{2\phi}{a}\right)$, where a is the transmission coefficient characteristic to the phase plate used, and cannot be changed unless the λ/4 filter is refitted through a tedious process of optical realignment.

Acknowledgments

We are grateful to Professor Masayuki Noguchi (Faculty of Medicine, University of Tsukuba) for providing us lung cancer cell samples (imaged in Figure 7) and for his helpful advice, and to Dr Naoki Fukutake (Nikon) for useful discussion. We gratefully acknowledge the supports from the Ibaraki Global Niche Top Companies Incubation Project and the Ichimura Foundation of New Technology.

References

[1] Frigault M M, Lacoste J, Swift J L and Brown C M 2009 Live-cell microscopy - tips and tools *J. Cell Sci.* **122** 753–67

[2] Popescu G, Park Y, Choi W, Dasari R R, Feld M S and Badizadegan K 2008 Imaging red blood cell dynamics by quantitative phase microscopy *Blood Cells, Mol. Dis.* **41** 10–6

[3] Mir M, Bhaduri B, Wang R, Zhu R and Popescu G 2012 Quantitative Phase Imaging *Prog. Opt.* **57** 133–217

[4] Popescu G 2011 *Quantitative phase imaging of cells and tissues* (New York: McGraw-Hill)

[5] Marquet P, Depeursinge C and Magistretti P J 2014 Review of quantitative phase-digital holographic microscopy: promising novel imaging technique to resolve neuronal network activity and identify cellular biomarkers of psychiatric disorders *Neurophotonics* **1** 020901

[6] Gustafsson M G L 2000 Surpassing the lateral resolution limit by a factor of two using structured illumination microscopy. *J. Microsc.* **198** 82–7

[7] Huang B, Jones S A, Brandenburg B and Zhuang X 2008 Whole-cell 3D STORM reveals interactions between cellular structures with nanometer-scale resolution *Nat. Methods* **5** 1047–52

[8] Rust M J, Bates M and Zhuang X 2006 Sub-diffraction-limit imaging by stochastic optical reconstruction microscopy (STORM) *Nat. Methods* **3** 793–6

[9] Betzig E, Patterson G H, Sougrat R, Lindwasser O W, Olenych S, Bonifacino J S, Davidson M W, Lippincott-Schwartz J and Hess H F 2006 Imaging Intracellular Fluorescent Proteins at Nanometer Resolution *Science (80-.).* **313** 1642–5

[10] Gaietta G, Deerinck T J, Adams S R, Bouwer J, Tour O, Laird D W, Sosinsky G E, Tsien R Y and Ellisman M H 2002 Multicolor and Electron Microscopic Imaging of Connexin Trafficking *Science (80-.).* **296** 503–7

[11] Hell S W and Wichmann J 1994 Breaking the diffraction resolution limit by stimulated emission: stimulated-emission-depletion fluorescence microscopy *Opt. Lett.* **19** 780–2

[12] Zernike F and F. 1942 Phase contrast, a new method for the microscopic observation of transparent objects part II *Physica* **9** 974–86

[13] Reichardt C 2005 Polarity of ionic liquids determined empirically by means of solvatochromic pyridinium N -phenolate betaine dyes *Green Chem.* **7** 339–51

[14] Teschke M and Sinzinger S 2009 Phase contrast imaging: a generalized perspective *J. Opt. Soc. Am. A* **26** 1015–21

[15] Rodrigo P J, Palima D and Glückstad J 2008 Accurate quantitative phase imaging using generalized phase contrast *Opt. Express* **16** 2498–509

[16] Glückstad J and Palima D 2009 *Generalized phase contrast : applications in optics and photonics* (Berlin: Springer)

[17] Popescu G, Ikeda T, Dasari R R and Feld M S 2006 Diffraction phase microscopy for quantifying cell structure and dynamics *Opt. Lett.* **31** 775–7

[18] Murphy D B and Davidson M W 2012 *Fundamentals of Light Microscopy and Electronic*

Imaging: Second Edition (Hoboken, NJ: Wiley-Blackwell)

[19] Salmon E D and Tran P 1998 High-resolution video-enhanced differential interference contrast (VE-DIC) light microscopy. *Methods Cell Biol.* **56** 153–84

[20] Lue N, Choi W, Popescu G, Ikeda T, Dasari R R, Badizadegan K and Feld M S 2007 Quantitative phase imaging of live cells using fast Fourier phase microscopy *Appl. Opt.* **46** 1836–42

[21] Mann C J, Yu L, Lo C-M and Kim M K 2005 High-resolution quantitative phase-contrast microscopy by digital holography *Opt. Express* **13** 8693–8

[22] Kemper B, Vollmer A, Rommel C E, Schnekenburger J and Bally G von 2011 Simplified approach for quantitative digital holographic phase contrast imaging of living cells *J. Biomed. Opt.* **16** 026014

[23] Shaked N T, Newpher T M, Ehlers M D and Wax A 2010 Parallel on-axis holographic phase microscopy of biological cells and unicellular microorganism dynamics. *Appl. Opt.* **49** 2872–8

[24] Cuche E, Bevilacqua F and Depeursinge C 1999 Digital holography for quantitative phase-contrast imaging *Opt. Lett.* **24** 291–3

[25] Tishko T V, Titar V P, Tishko D N and Nosov K V 2008 Digital holographic interference microscopy in the study of the 3D morphology and functionality of human blood erythrocytes *Laser Phys.* **18** 486–90

[26] Tishko T V, Tishko D N and Titar V P 2012 Combining the polarization-contrast and interference-contrast methods for three-dimensional visualization of anisotropic microobjects *J. Opt. Technol.* **79** 340–3

[27] Pluta M 1993 Variable phase contrast microscopy: simplified polanret system *Opt. Eng.* **32** 3215–22

[28] Richards O W 1973 The Polanret variable densiphase microscope *J. Microsc.* **98** 67–77

[29] Osterberg H and Pride G E 1950 The Measurement of Unresolved, Single Particles of Uniform Thickness by Means of Variable Phase Microscopy *J. Opt. Soc. Am.* **40** 64–73

[30] Osterberg H 1947 The Polanret Microscope *J. Opt. Soc. Am.* **37** 726–30

[31] Otaki T 2000 Artifact Halo Reduction in Phase Contrast Microscopy Using Apodization *Opt. Rev.* **7** 119–22

[32] Garcia-Sucerquia J, Xu W, Jericho S K, Klages P, Jericho M H and Kreuzer H J 2006 Digital in-line holographic microscopy *Appl. Opt.* **45** 836–50

[33] Vainrub A, Pustovyy O and Vodyanoy V 2006 Resolution of 90 nm (λ/5) in an optical transmission microscope with an annular condenser *Opt. Lett.* **31** 2855–7

[34] Goodman J . 2005 *Introduction to Fourier Optics, Third Ed.* (Englewood, Co: Roberts & Co)

[35] Shiba-Ishii A, Kim Y, Shiozawa T, Iyama S, Satomi K, Kano J, Sakashita S, Morishita Y and Noguchi M 2015 Stratifin accelerates progression of lung adenocarcinoma at an early stage *Mol. Cancer* **14** 1–6

[36] Shiba-Ishii A, Hong J, Hirokawa T, Kim Y, Nakagawa T, Sakashita S, Sakamoto N, Kozuma Y, Sato Y and Noguchi M 2019 Stratifin inhibits SCFFbw7 formation and blocks

ubiquitination of oncoproteins during the course of lung adenocarcinogenesis *Clin. Cancer Res.* **25** 2809–20

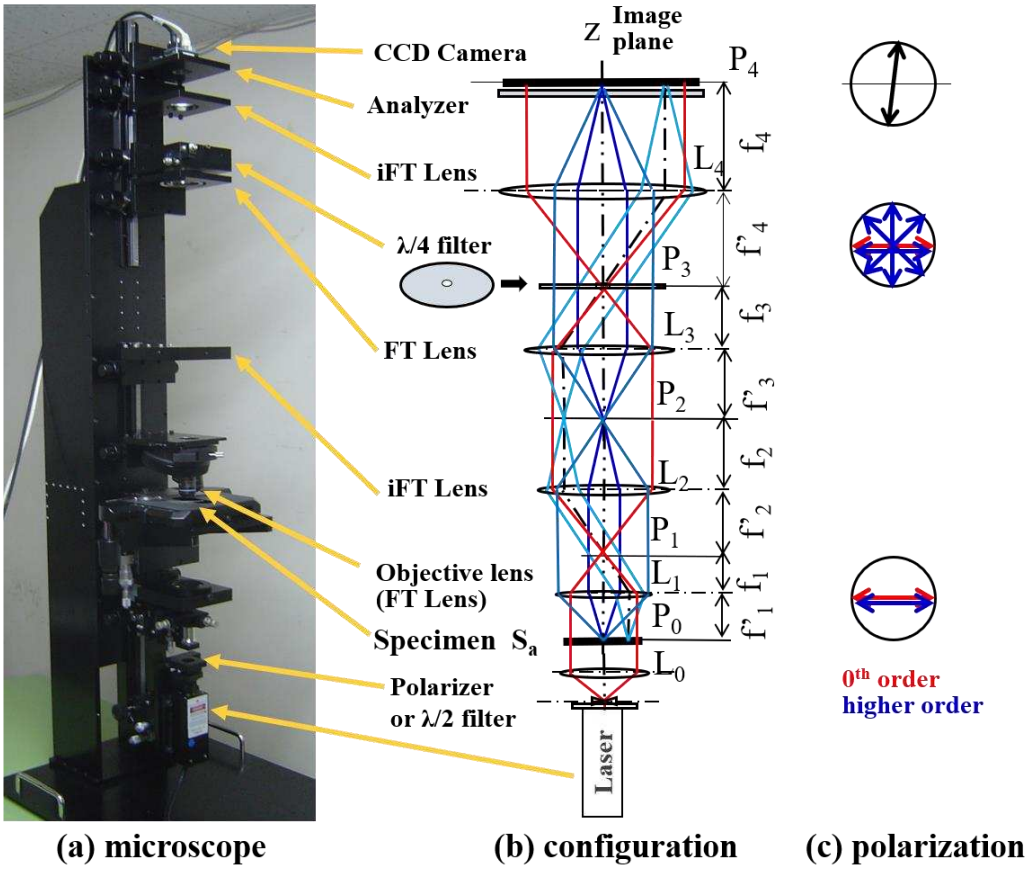

Fig. 1. (a) Photo of our microscope. (b) Optical configuration of our microscope. (c) A schematic representation of polarization changes and contrast tuning principles.

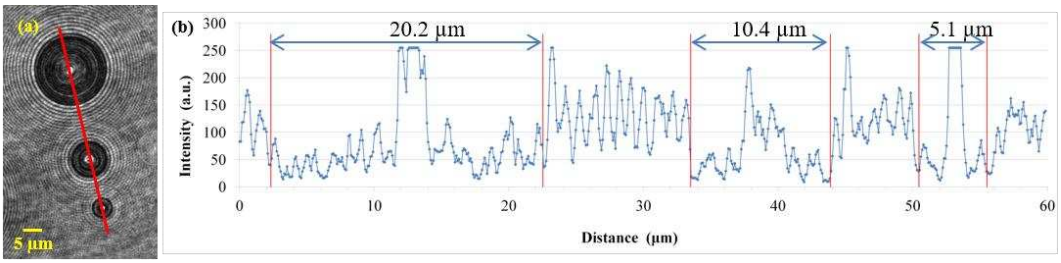

Fig. 2. (a) Imaging a mixture of mono-disperse polystyrene latex spheres of three different diameters (5.0, 10.3, and 20.3 µm) under the following conditions: optical magnification： 94.4×; λ = 532 nm; camera: 4000 × 2672 (9µm/pixel); whole view: 381 µm × 255 µm; resolution: 95.3 nm/pixel. The red line is along which the intensity profile in (b) is recorded. (b) Intensity profiles of monodisperse polystyrene latex particles of three different diameters (5.0, 10.3 and 20.3 µm) along the red line indicated in Figure 2. The relative intensity has been calculated from the grey scale values.

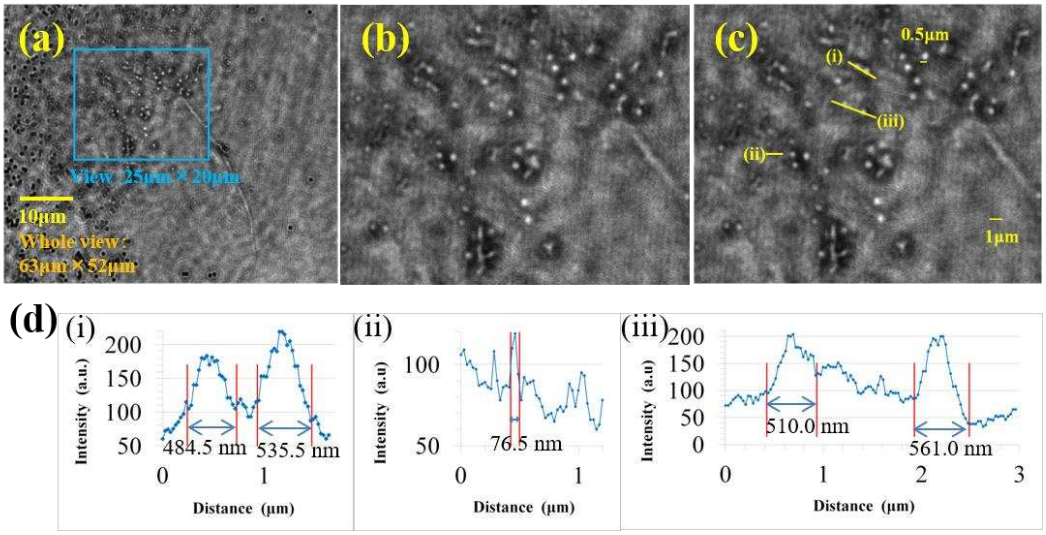

Fig. 3. (a) Imaging of 0.5 µm (500 nm) polystyrene latex spheres mixed with 80 nm gold spheres under the following conditions: optical magnification: 135×; λ = 532 nm; camera: 2464 × 2056 pixel (3.45 µm/pixel), whole view: 63 µm × 52 µm; resolution: 25.5nm/pixel. (b) Expansion of the area within the blue rectangle in (a), covering 25 µm × 20 µm. (c) Annotation of Fig 3(b); the line profiles in Fig. 3(d) are recorded along the three yellow lines: (i), (iii): 500 nm PL spheres; (ii): an 80 nm gold sphere. (d) Intensity profiles of monodisperse polystyrene latex particles (500 nm) and monodisperse gold particles (80 nm) along the lines ((i)-(iii)) indicated in Fig. 3(c). The relative intensity has been calculated from the grey scale values. The pixel numbers roughly corresponding to the radii are shown for comparison.

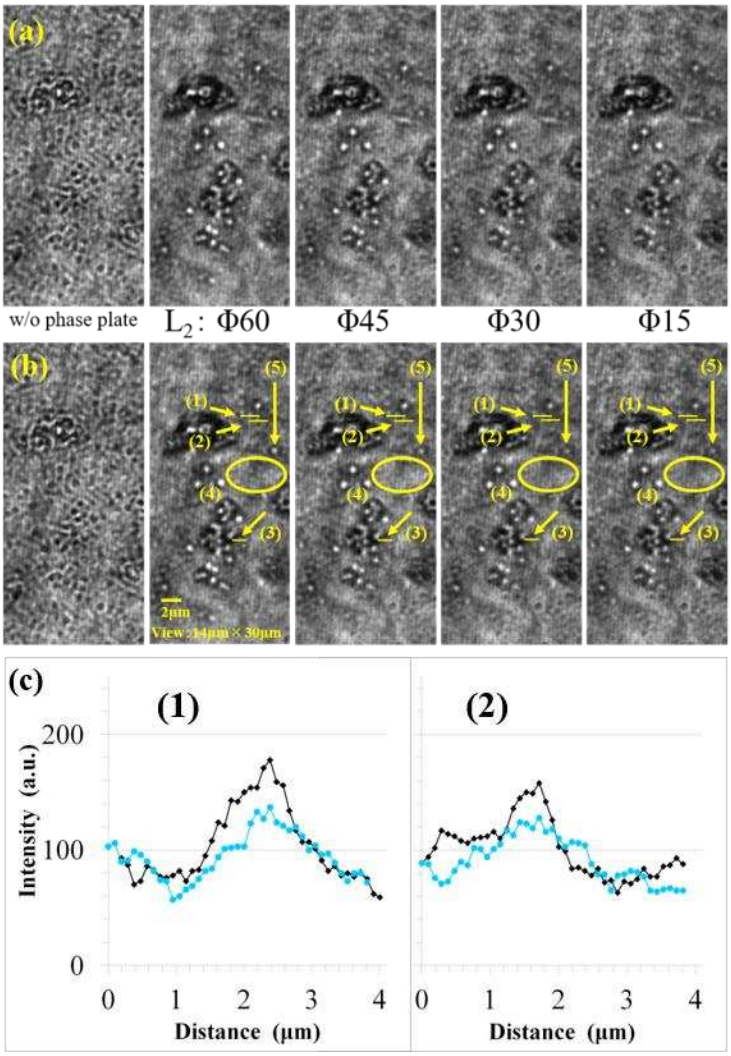

Fig. 4. (a) Imaging of a mixture of 80 nm gold nanoparticles and 500 nm polystyrene latex spheres without the phase plate (left) and with the phase plate with decreasing lens diameter (from left to right) imaged under the following conditions: optical magnification: 135; camera: 2464 × 2056 pixels (3.45 μm/pixel); whole view: 63 μm × 52 μm; resolution: 25.5 nm/pixel. 14 μm × 30 μm sections were extracted and shown here. (b) The same image as (a) with annotations: (1)-(4):80 nm; (5): 500 nm. (c) Intensity profiles of an 80 nm gold nanoparticle (Fig. 4(a)(b), along (1) and (2)) with 60 mm FT lens (black) and with an aperture (15 mm) inserted to block higher-order scattered beams (blue).

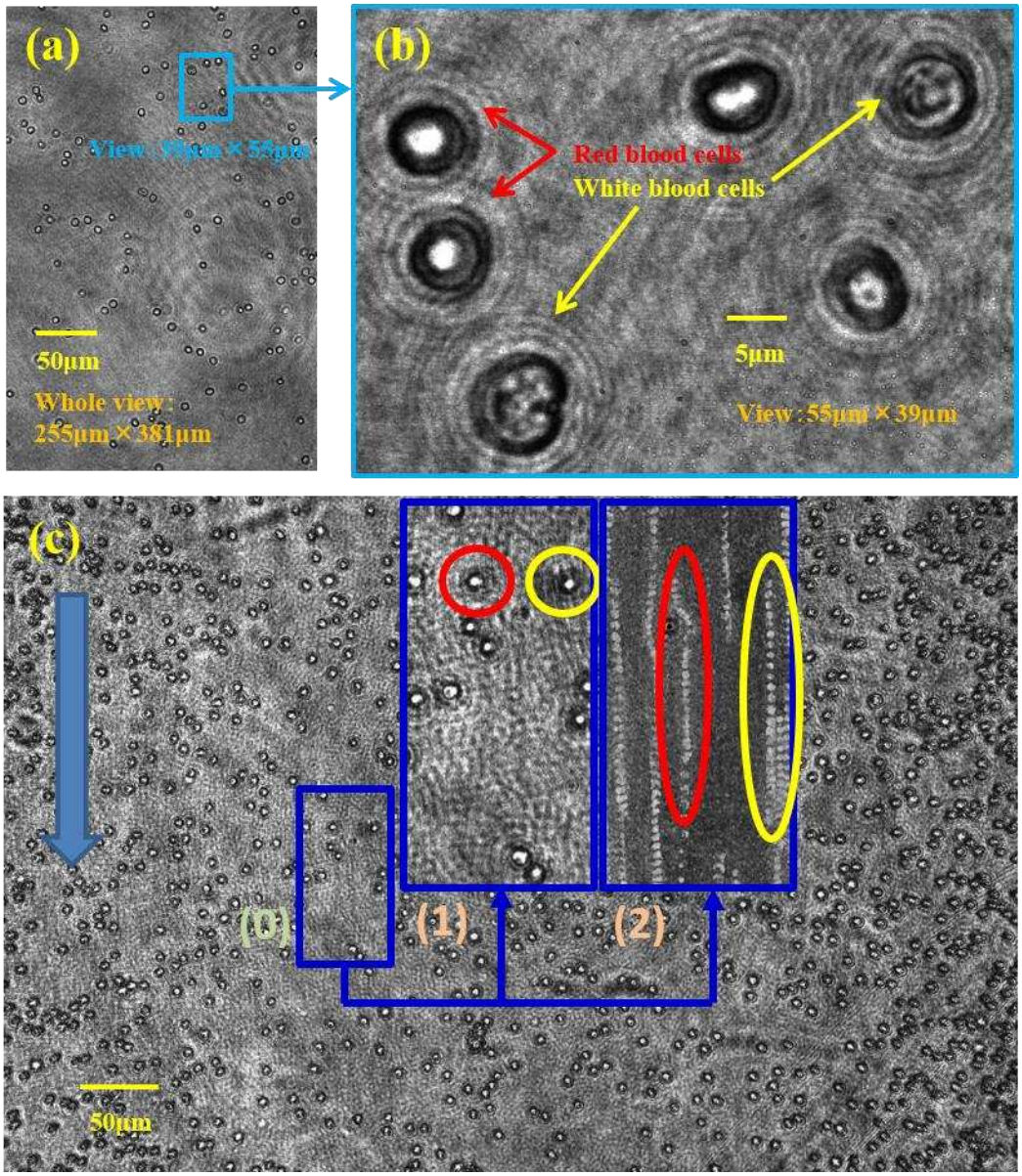

Fig. 5. (a) Imaging blood cell sample (a) with the whole view 255 μm × 381 μm. (b) Expanded view. (c) Application to flow cytometry of human blood cells. The direction of the flow is indicated by a blue arrow. Whole view: 648 μm× 433 μm. Inset (1) expanded still image from the area within the blue rectangle (0); (2) cell flow dynamics visualized by snapshots taken every 5 fps.

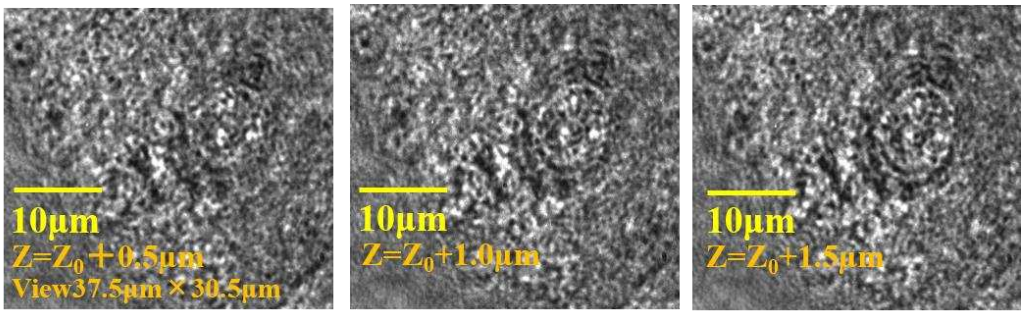

Fig. 6. Human oral epithelial cells imaged along the variation of focal depth along the optical axis (Z) by an interval of 0.5μm from the original position (Z_0)

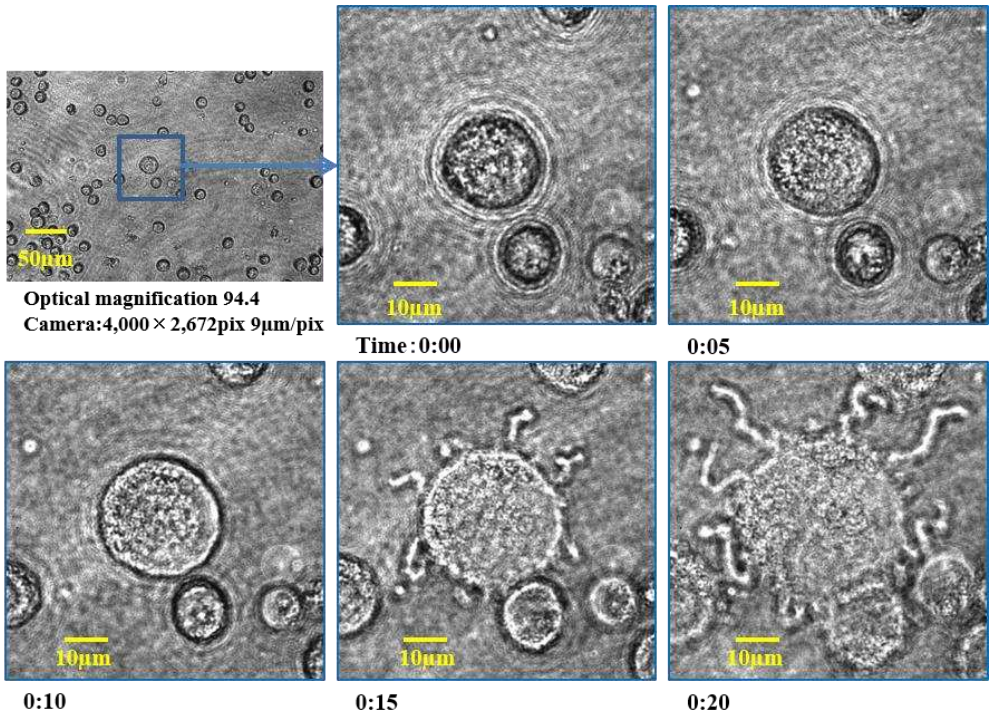

Fig. 7. Cancer cell dynamics. The motion along time of human lung cancer cells from the A549 cell line, provided by Professor Masayuki Noguchi of the University of Tsukuba. Magnified images (covering 73 μm × 73 μm) were taken every five minutes from the original (top-left) with optical magnification 94.4×, whole view: 381 μm × 255 μm.

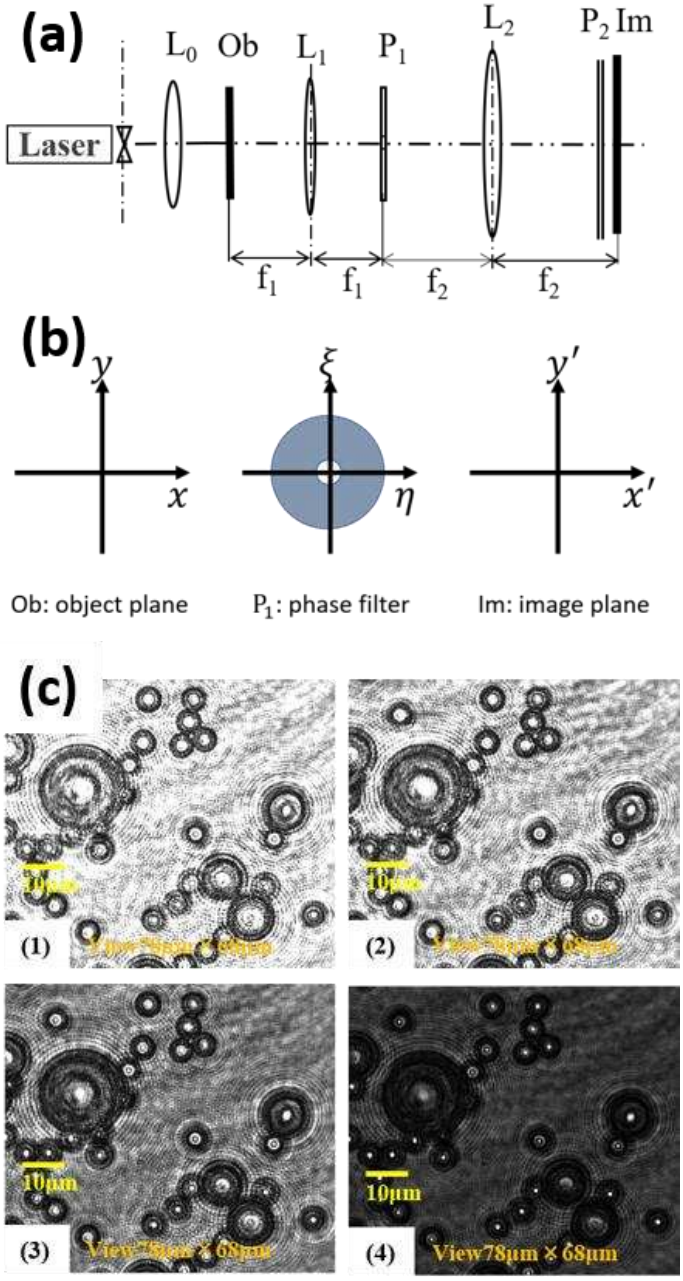

Fig. 8. Demonstration of the tunability of image contrast by the rotation of the polarizer. (a) The simplified optical setup for theoretical analysis. (b) Definition of coordinate system used in the theory. (c) Demonstration of contrast optimization using images of polystyrene latex spheres of three different diameters (5, 10.3 and 20.3 μm) taken by our microscope (78 μm × 68μm section from the original 612 μm × 409 μm images recorded with 153 nm /pixel). The angles ($\alpha + \pi/4$) in Eq. (9) are (1) 0, (2) $\pi/6$, (3) $\pi/4$ and (4) $\pi/3$, respectively.